Preparation of Ni and NiCu/Yttria-Stabilized Zirconia Model Electrodes with Optimized Triple-Phase Boundary Geometry for Fundamental Operando Spectroscopic Studies

Christoph W. Thurner, Leander Haug, Daniel Winkler, Victoria Zarth, Johannes Glätzle, Kevin Ploner, Jonathan Schäfer, Simon Penner,* and Bernhard Klötzer

Solid oxide cell technologies play a pivotal role in the realm of renewable energy storage, guiding us through the journey toward decarbonization. Understanding how electrocatalytic materials behave under high-temperature conditions is an absolute necessity to push these technologies forward. Operando spectroscopic investigations, such as near-ambient pressure X-ray photoelectron spectroscopy (NAP–XPS), offer insights into the chemical nature of active working electrodes, including the dynamic response of redox states and adsorbate chemistry to changing electrochemical conditions. Mixed ceramic–metallic electrodes exhibit a limited region with electrochemically active triple-phase-boundary (TPB) sites, which are located close to the electrolyte/electrode interface. To monitor this specific region spectroscopically, metallic (Ni) and bimetallic (NiCu) network-like structures are synthesized on a yttria-stabilized zirconia electrolyte and the electrochemical state and performance are studied by using operando NAP–XPS. In the experiments, the surface oxidation states under different polarizations are revealed, the gas composition dependent Nernst shift is confirmed, electrocatalytic activities are unraveled, and hydrogen evolution is correlated with the applied potential. The findings demonstrate, the effectiveness of thin-film model cells with spectroscopically accessible TPB regions for probing interfacial states and electrochemical processes. The obtained fundamental knowledge can provide valuable insights for the advancement of renewable energy storage technologies.

1. Introduction

Knowledge-based improvement of solid oxide cell (SOC) technologies utilized for renewable energy storage via electrolysis of water and/or CO_2 and reversible power release via fuel cell operation are of continuing interest.[1,2] For facilitating decarbonization, power-to-X technologies (X comprises, e.g., H_2, syngas, or synthetic fuels) will play a central role in this transition.[3] The understanding of advanced electrocatalytic materials and their knowledge-based improvement is fundamental in this perspective. Therefore, the study of high-temperature surface-processes during SOC operation is of ultimate importance. In situ and operando spectroscopic investigations based on surface-sensitive methods, such as near-ambient pressure X-ray photoelectron spectroscopy (NAP–XPS) or Raman spectroscopy, can provide a detailed insight into the chemical nature of the working electrode (WE) (i.e., electrode redox state, electrocatalyst poisoning, or adsorbate chemistry, respectively).[4–9] Consequently, the direct observation of the electrochemically active zone is of central importance, as it provides the opportunity to derive scientific conclusions regarding the processes at the electrified gas/electrolyte/electrocatalyst interface (denoted as triple-phase boundary

C. W. Thurner, L. Haug, D. Winkler, V. Zarth, S. Penner, B. Klötzer
Institute of Physical Chemistry
University of Innsbruck
Innrain 52c, 6020 Innsbruck, Austria
E-mail: simon.penner@uibk.ac.at

The ORCID identification number(s) for the author(s) of this article can be found under https://doi.org/10.1002/sstr.202300414.

J. Glätzle, J. Schäfer
R&D Department
Ceratizit Austria GmbH
Metallwerk-Plansee-Strasse 71, 6600 Reutte, Austria

K. Ploner
Analytical Department
Plansee SE
Metallwerk-Plansee-Strasse 71, 6600 Reutte, Austria

**ADVANCED
SCIENCE NEWS**

www.advancedsciencenews.com

**small
structures**

www.small-structures.com

[TPB]) and to distinguish them from conventional thermochemically driven processes on electrochemically less active or inactive, yet still chemically reactive, cermet regions.

Generally, mixed (oxide ion and electron) conducting interfaces can represent electrochemically active zones, rendering the localized investigation of charge-transfer-driven adsorbate and redox chemistry particularly intriguing. For dense mixed-ionic-electronic-conductor (MIEC) electrode films (e.g., consisting of phase-pure perovskites or doped ceria materials), the electrochemically active area is largely located at the topmost surface layer; hence, mechanistic in situ studies of MIEC oxide films by NAP–XPS are quite common.[10,11] However, for ceramic–metallic (cermet) electrodes (e.g., Ni–yttria-stabilized zirconia (YSZ)), the electrochemically active zone is largely restricted to the 3D-porous cermet interface region in vicinity of the dense solid electrolyte. The electrochemical processes occur necessarily within this zone, which must feature both sufficient ionic and electronic conductivity, while the outer electrode surfaces and interfaces being little or not accessible for oxygen ion exchange.[12,13] Therefore, the electrochemically active zone of an extended porous cermet electrode is spectroscopically inaccessible by means of surface sensitive analysis by NAP–XPS.

Consequently, we focused on the design of sophisticated ultrathin or quasi-2D-structured model systems, exhibiting most of their active sites within the information depth of NAP–XPS. A well-established approach to fabricate cermet-like 2D metal/electrolyte interfaces is photolithography,[14] typically aiming at regularly structured metallic films with several 100 nm in thickness and a domain size in the μm regime deposited on top of a solid electrolyte.[15] Nevertheless, this type of meso-scaled, nonporous model electrode systems is mainly used to extract fundamental mechanistic knowledge (e.g., distinction of preferential surface or bulk paths[16]) and allows only for very limited TPB dimensions in NAP–XPS investigations.[17] Thus, such concepts cannot fully meet the requirement of maximized TPB dimensions for spectroscopically investigable metal/electrolyte interfaces, which rather requires a nanoscaled TPB environment. Additionally, they are hardly comparable with technically applicable porous electrodes, especially those optimized by Ni–YSZ infiltration techniques,[18] which exhibit randomly orientated and finely dispersed grains in the nanoscale regime.

However, network-like percolated metallic Pt/YSZ structures were already successfully prepared at the nanoscale via a physical vapor deposition approach and subsequent thermal annealing.[19] In terms of their quasi-2D pore dimensions, it was shown that such 2D model electrodes combine the structural characteristics of a meso- and nanoscaled TPBs (e.g., film grain boundaries or cavities).[19] As the analogous preparation of this type of nanoscaled network electrodes was not reported for other, industrially more relevant cermets, such as Ni/8-YSZ, the main scope of this work is 1) to show the successful preparation of the analogous metallic Ni and bimetallic NiCu network-like structures on YSZ; and 2) to present experimental evidence for the characterization of industrially relevant model electrodes via electrochemical operando NAP–XPS combined with mass spectrometry (MS). With respect to the eventual choice of materials and conditions, pure Ni serves as a "proof of principle" reference

material studied at realistic temperatures up to 773 K in a H_2/H_2O mixture of 1:99 at 1 mbar total pressure, and its characterization provides the basis for the analysis of the related NiCu network on YSZ.
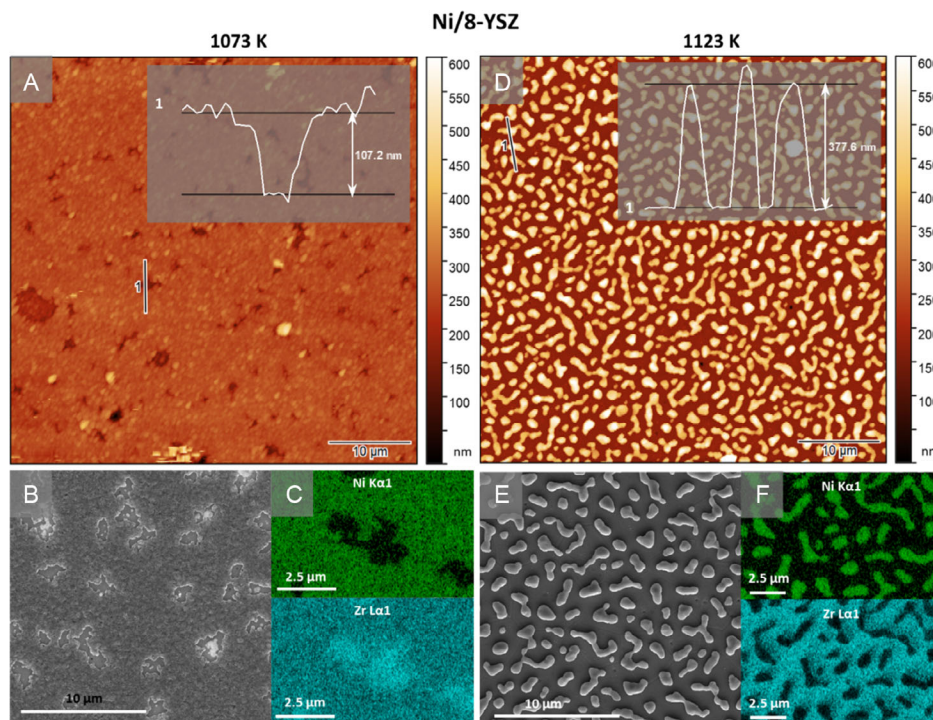
2. Results and Discussion

2.1. Model Electrode Characterization

A complementary characterization of the thin-film electrodes by microscopic and spectroscopic techniques was performed to investigate the structural development of the thin-film structures and their chemical composition as a function of annealing temperature. The AFM image of the polished, flat YSZ substrate surface is shown in Figure S2, Supporting Information. **Figure 1** summarizes the results derived from AFM, SEM, and EDXS analysis for a Ni/8-YSZ thin-film electrode annealed at 1073 K (panels A, B, and C, respectively) and 1123 K (panels D, E, and F respectively). From each AFM image (panels A and D), a height profile was extracted and illustrated as an inset in the respective panel.

After annealing of the originally continuous Ni thin film at 1073 K, an electron-conducting but increasingly porous thin-film structure is formed. The regions with apparent pits, which expose the underlying YSZ solid-electrolyte surface, were at first characterized by AFM. A height profile scan trough such a pit region shows a roughly 100 nm deep crater, which is in good agreement with the deposited film thickness. The pit hole shape, the surrounding Ni domains as well as the local chemical composition were resolved by conducting SEM combined with EDXS (Ni $K\alpha_1$ and Zr $L\alpha_1$) characterization (panels B and C), confirming the structural interpretation derived from AFM.

Analysis after annealing at 1173 K demonstrates that the Ni-thin-film agglomerates toward isolated Ni islands on top of the polished YSZ substrate. A height profile reveals a Ni-island growth up to ≈400 nm. In the respective SEM images (panel E in Figure 1 and S3, Supporting Information), the emerging YSZ grain boundaries are visible, indicated by their characteristic polygonal shape with a grain size of 2–10 μm.[19] EDXS confirms the assignment of the isolated Ni islands formed on the YSZ substrate (panel F).

The characterization of the 2D-structured $Ni_{80}Cu_{20}$ thin film was carried out by utilizing the same methodology (AFM, SEM, and EDXS) as for pure Ni, providing a consistent insight into the evolution of the film structure as a consequence of the applied annealing temperature (**Figure 2**). The $Ni_{80}Cu_{20}$ thin film already starts to agglomerate at an annealing temperature of 1043 K, which is 30 K lower than for pure Ni. In addition, the release of the YSZ substrate was found to be more pronounced compared to the pure Ni thin film. A height profile shows a film thickness of approximately 100 nm and some agglomerated NiCu at the edges of the pit hole. Furthermore, due to the annealing procedure, the NiCu surface was found to be quite rough, while the polished YSZ surface remains smooth. The local chemical composition of the NiCu domains was mapped by EDXS of the Ni $K\alpha_1$, Zr $L\alpha_1$, and Cu $K\alpha_{1,2}$ edge (panel C), confirming the NiCu intermixing at least with respect to the lateral resolution of EDXS (≈200 nm for Cu K radiation at 15 kV acceleration voltage).

ADVANCED
SCIENCE NEWS
www.advancedsciencenews.com

small
structures
www.small-structures.com

Figure 1. Microscopic A,D) atomic force microscopy (AFM) and B,E) scanning electron microscopy (SEM) and C,F) energy-dispersive X-ray spectroscopic (EDXS) investigations of the Ni/8-YSZ thin-film electrode annealed at 1073 K (left) and 1123 K (right). A height profile embedded in the respective AFM image provides additional information on the local structure of the Ni thin film as a function of annealing temperature.
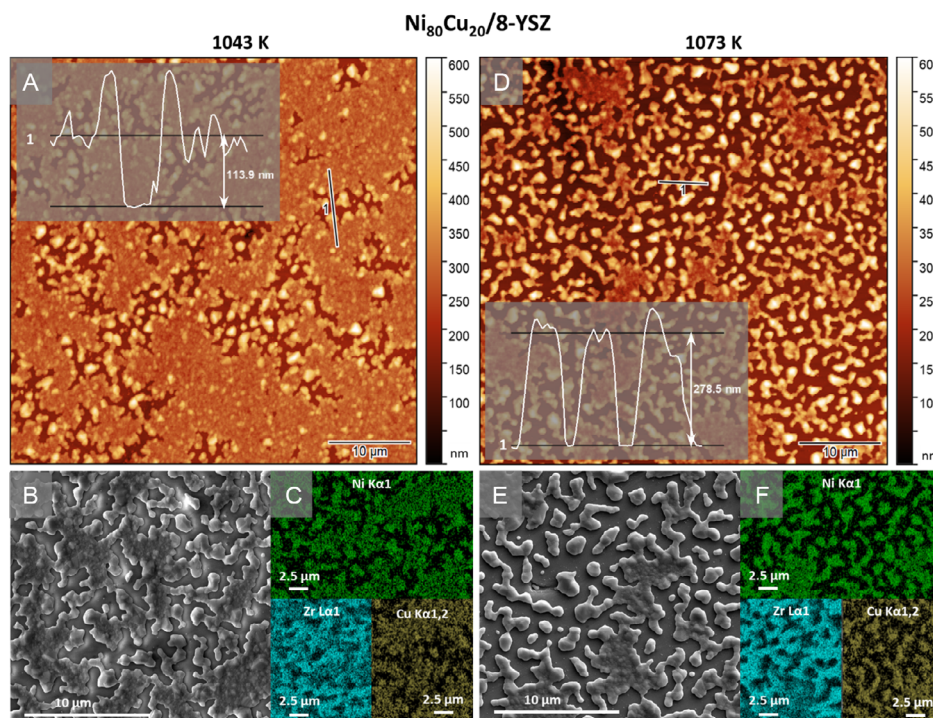
Figure 2. Microscopic A,D) AFM and B,E) SEM and C,F) spectroscopic (EDXS) analysis of the $Ni_{80}Cu_{20}$/8-YSZ thin-film electrode annealed at 1043 K (left) and 1073 K (right). A height profile embedded in the respective AFM images (panels A and D) provides additional information on the local structure of the $Ni_{80}Cu_{20}$ thin film in vicinity of the pore/grain-boundary regions as function of annealing temperature.

**ADVANCED
SCIENCE NEWS**

www.advancedsciencenews.com

**small
structures**

www.small-structures.com

By increasing the annealing temperature 30–1073 K, the percolated thin film breaks up, which leads to the loss of electron conductivity and the formation of isolated NiCu islands. The height profile extracted from the AFM experiment indicates a perpendicular particle growth up to ≈300 nm, giving rise to quite mobile Ni and Cu atoms present at this temperature. The AFM results were confirmed by SEM and EDXS analysis (panels *E* and *F*).

A quantification of the surface composition by XPS and a comparable SEM image analysis of the YSZ surface coverage was conducted for the electrochemically applied thin-film electrodes (see Figure S4 and S5 and Table S1, Supporting Information). In addition to the YSZ surface area determination, which confirms the controlled de-wetting of the metallic thin film, the analysis of the X-ray photoelectron (XP) spectra validates the successful intermixing of Ni and Cu according to the expected $2p_{3/2}$ peak

positions of the $Ni_{80}Cu_{20}$ alloy. Especially the Cu $2p_{3/2}$ spectrum exhibits a binding energy (BE) shift of −0.2 eV with respect to the metallic Cu(0) reference position of 932.8 eV, in agreement with ref. [20].

2.2. Potential-Controlled Surface States

An electrochemical proof of principle in situ XPS experiment illustrating the benefits and strengths of the prepared metallic network-like or holey thin-film systems deposited on a gas-tight YSZ solid electrolyte was carried out on the $Ni_{80}Cu_{20}$ electrode. The respective results are summarized in **Figure 3**. The experiment was set up as follows. 1) The SOC was heated to 773 K in 1 mbar $H_2:H_2O = 1:99$ atmosphere. 2) A cyclic voltammogram (CV, green trace, *A–F* anodically increasing and *E′–A′* cathodically decreasing polarizations) with a scan rate of 50 mV s^{-1} was
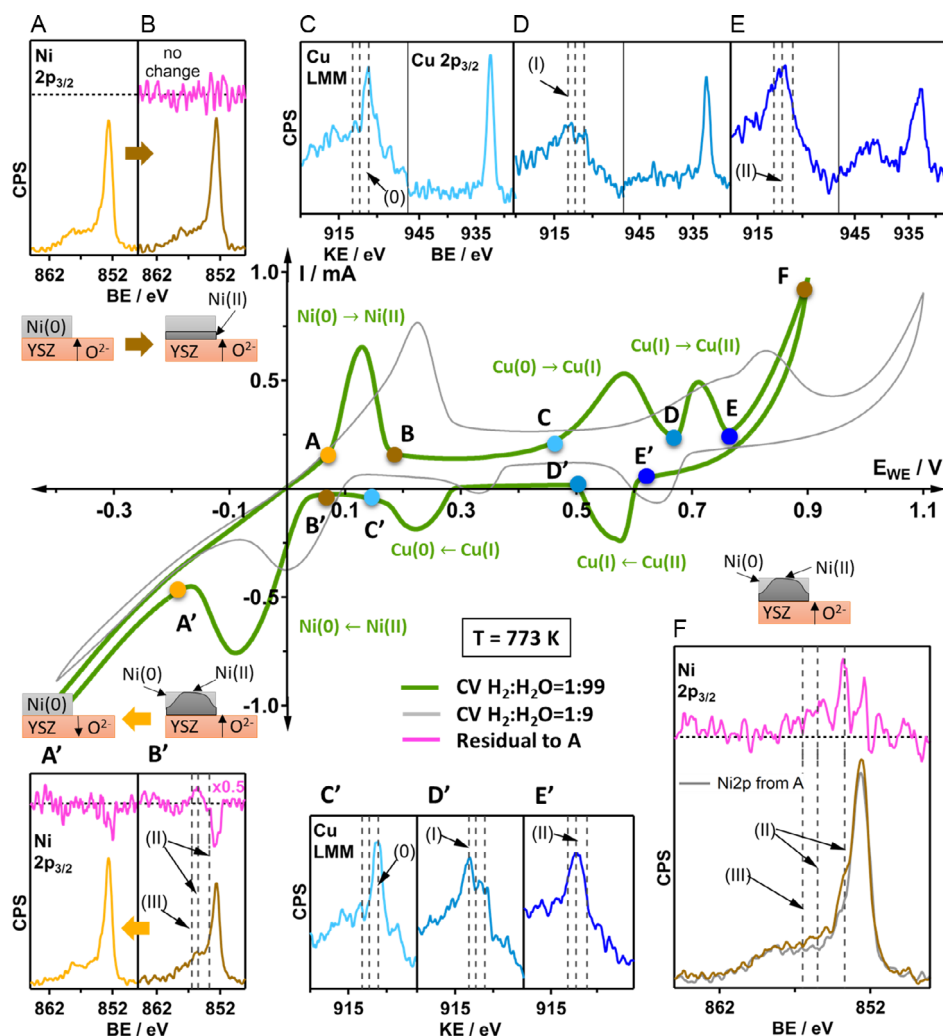
Figure 3. In situ Ni 2p, Cu 2p XP, and Cu LMM Auger spectra recorded under chronoamperometric (CA) conditions at the indicated voltages of the green-colored cyclic voltammogram (CV) shown in the middle of the viewgraph, revealing the polarization-dependent oxidation states of the alloyed $Ni_{80}Cu_{20}$ electrode. The shown CVs were recorded separately at a continuous sweep rate of 50 mV s^{-1} at 773 K in either 1 mbar $H_2:H_2O = 1:99$ atmosphere (green trace) or in 1 mbar $H_2:H_2O = 1:9$ atmosphere (gray trace). Thereafter, the spectra were collected under the otherwise identical experimental conditions of the green CV by keeping the potential constant at the respective color-coded values (anodic branch: A = 80, B = 190, C = 460, D = 680, E = 760, and F = 900 mV; cathodic branch: E′ = 610, D′ = 515, C′ = 135, B′ = 85, and A′ = −195 mV). To visualize the partial Ni oxidation at anodic potentials, residuals of the respective background-corrected Ni $2p_{3/2}$ spectra were obtained by subtraction of the Ni(0) spectrum of panel A (violet traces).

ADVANCED
SCIENCE NEWS
www.advancedsciencenews.com

small
structures
www.small-structures.com

recorded to identify distinct polarization states corresponding to pronounced current density responses in the CV. These features are associated, e.g., with a change in the alloy component's oxidation states. 3) To resolve these oxidation states spectroscopically in detail, the cell was polarized in a stepwise manner under chronoamperometric (CA) conditions at each characteristic anodic and cathodic sweep potential. After an equilibration period of the current of $\approx$3 min, XP and Auger spectra of the Ni $2p_{3/2}$, Cu $2p_{3/2}$, and Cu LMM regions were recorded. 4) Based on thermodynamic considerations, a second CV (gray trace) was taken after changing the atmosphere to 1 mbar H_2:$H_2O = 1$:9, to confirm an anticipated Nernst shift due to the H_2-enriched atmosphere.

The discussion is structured according to the anodic sweep potentials (A–F) followed by the cathodic branch (E'–A'). To highlight minor changes of the Ni oxidation state most efficiently, a differential trace ("residual") obtained by subtraction of the respective Ni $2p$ spectrum of pristine pure Ni(0) (panel A) is displayed. The anodic peak in the CV between $A = 80$ mV and $B = 190$ mV can be associated with the oxidation of Ni(0) to Ni(II), although no change was detected in the Ni $2p_{3/2}$ region by going from A to B. This can be explained by the fact that the initial Ni oxidization toward NiO is restricted to the interface between the thin film and the YSZ.[17] Due to the low inelastic mean free path (IMFP) of the Ni $2p$ photoelectrons ($\approx$1.08 nm),[21] the geometrically hidden interfacial oxidation cannot be detected with XPS underneath a 100 nm thick metallic film, but can be observed in the CV due to the associated O^{2-}-electron-transfer reaction. Hence, the obtained XPS results are showing unchanged (i.e., confirmed by the residual) metallic Ni in agreement with ref. [17].

At 460 mV (point C), metallic Cu is still predominant, as confirmed by the characteristic Cu LMM Auger spectra (Cu(0) = 918.9 eV) and the Cu $2p_{3/2}$ region (BE = 932.6 eV). At D (680 mV), Cu is oxidized to Cu(I), which is mainly visible in the Cu LLM Auger region (Cu(I) = 916.8 eV), whereas in the Cu $2p_{3/2}$ region, Cu(0) and Cu(I) cannot be distinguished.[22] Although the two oxidation peaks of Cu (Cu(0) $\rightarrow$ Cu(I) and Cu(I) $\rightarrow$ Cu(II)) are almost overlapping in the CV, the respective reduction peaks are well separated. This is similar to the redox behavior of Cu in aqueous electrolyte at room temperature.[23] Hence, the intermediate Cu(I) signal becomes better visible in the cathodic branch (see D'). By increasing the potential further to $E = 760$ mV, the oxidation of Cu toward the +II state is clearly evidenced by the respective Cu LMM (KE = 917.7 eV) and Cu $2p_{3/2}$ data.

Interestingly, by jumping to point F (900 mV), so far still mostly metallic surface Ni partially changes its oxidation state toward +II. However, a minor contribution of a + III species cannot be excluded based on the calculated residual. The literature-known peak positions for Ni(II) and Ni(III) species (e.g., NiO, Ni(OH)$_2$, γ-NiOOH, and β-NiOOH) correspond to three main contributing signals (BE = 853.7 and 855.5 eV for Ni(II) and 856.5 eV for Ni(III))[24,25] and are indexed as dashed lines in the respective panels. To clearly visualize the changed Ni peak shape recorded at 900 mV (brown trace), the signal recorded in A (i.e., the one used for the residual calculation) is plotted as gray trace in panel F. The residual indicates pronounced intensity exactly at the characteristic BEs corresponding

to the Ni(II) components and thus confirms the interpretation that oxidized Ni species start to accumulate also at the XPS-accessible regions of Ni.

However, it appears counterintuitive that the metallic component in the Ni $2p$ signal (main peak at 852.7 eV, brown trace) is rather increased as compared to the spectra recorded in A. Based on the difference in density of the Ni species (ρ(Ni) = 8.91 g cm^{-3} and ρ(NiO) = 6.67 g cm^{-3}), this phenomenon is most likely associated with a surface wetting process. As the oxidation of Ni starts at the Ni/YSZ interface,[17] the metallic Ni on top of the NiO interlayer layer also expands, which results in an intermediate increase in intensity of the metallic Ni component in F. In contrast, a more pronounced oxidation of Ni at the surface finally triggers a decrease of the Ni(0) signal in B'. Figure S6, Supporting Information, shows the background-corrected Ni $2p_{3/2}$ peak heights measured at 825.7 eV and plotted as a function of anodic potential, confirming the interplay of surface wetting versus oxidation. An increase in the peak height of the metallic Ni component was determined from points A to D (i.e., density difference driven wetting), followed by a decrease from D to F due to a more and more pronounced oxidation of surface Ni. Nevertheless, the peak height in F converges at a higher level than in A.

By going from E' to C', the reduction of the different oxidation states of Cu (i.e., Cu(II) $\rightarrow$ Cu(I) $\rightarrow$ Cu(0)) is resolved in the respective spectra of the Cu LMM Auger region.

Finally, a change from partially oxidized Ni toward metallic Ni is obvious between B' and A'. The residual in B' is a strong indicator for still persisting oxidized Ni, showing a decrease in the Ni(0) main peak and pronounced intensity in the BE region of the Ni(II) features. By jumping from B' to A', a purely metallic Ni(0) peak was regenerated, as confirmed by the respective residual and the reestablished peak intensity as compared to the initial spectrum of panel A.

In summary, the spectroscopic measurements prove how powerful in situ NAP–XPS actually is, as they perfectly complement the electrochemical redox features of the CV experiment. Despite Ni being less noble than Cu, it is evident that Cu undergoes full oxidation at the surface, while surface Ni stays mainly metallic. We attempt to explain this observation by the superior hydrogen adsorption kinetics of metallic Ni relative to Cu.[26] The associated preferential reduction of Ni near-surface regions by the added H_2(g) (H_2:$H_2O = 1$:99) would be rather expected for a nonstatistical Ni–Cu surface distribution at the alloy surface, implying spatially separated Ni and Cu domains. While we cannot offer specific experimental evidence for the existence of such domains on the basis of in situ microscopic techniques, it is worth noting that pronounced gas-phase and temperature-dependent segregation processes of Ni versus Cu have been reported under non-electrochemical CO_2 hydrogenation conditions.[27] Trends of the Ni versus Cu surface composition become also visible in our in situ Ni $2p_{3/2}$ and Cu $2p_{3/2}$ integral area data. Specifically, we found a tendency for preferential Cu surface segregation under oxidizing/anodic conditions (Figure S7, Supporting Information, points C–F), which appears to be largely reversible with some hysteresis, at least within the available information depth (excitation energy of 1486.6 eV, IMFP $\approx$1.08 nm for Ni). Furthermore, the data suggest that after the anodic segregation of oxidic Cu species, the reverse process is

linked to the conversion of oxidic Ni species toward metallic Ni (Figure S7, Supporting Information, points $B'-A'$). Based on these findings, it seems plausible that oxidized Cu domains preferentially segregate within an otherwise metallic Ni environment on the surface. These findings agree with a recent NAP–XPS study,[27] presenting Cu segregation as Cu oxide from a $Ni_{50}Cu_{50}$ alloy under O_2 atmosphere and resegregation under H_2 atmosphere at 673 K.

To understand the anodic shift of the CV obtained at the higher partial pressure of H_2 (light gray trace in Figure 3), one needs to consider the thermodynamics of the oxidation reaction of a metal M to a metal oxide MO in water vapor (Equation (1)). As the coexisting oxidic and metallic components can be regarded as single and pure solid phases, their activity can be assumed as unity. Thus, the oxidation potential E according to the Nernst equation (Equation (2)) is only a function of the partial pressures p of the respective gases, specifically of the ratio of the water and hydrogen partial pressures:

$$M + H_2O \rightleftharpoons MO + H_2 \tag{1}$$

$$E = E^0 + \frac{RT}{zF} \cdot \ln \prod_j \left(\frac{p_j}{p^0} \right)^{\nu_j} \tag{2}$$

During the first CV experiment, the partial pressures of H_2O and H_2 amount to 0.99 and 0.01 mbar, which results in an oxidation potential E_I. After changing the gas mixture to $H_2O = 0.90$ mbar and $H_2 = 0.10$ mbar, the potential shifts toward E_{II}. The difference to both potentials ΔE_{II-I} can be expressed via Equation (3):

$$\Delta E_{II-I} = \frac{RT}{zF} \cdot \ln \frac{\left(\frac{p_{II,H2O}}{p^0} \right)^{-1} \left(\frac{p_{II,H2}}{p^0} \right)^{1}}{\left(\frac{p_{I,H2O}}{p^0} \right)^{-1} \left(\frac{p_{I,H2}}{p^0} \right)^{1}} \tag{3}$$

As the experiment temperature remained unchanged overtime in both gas mixtures, E^0 can be considered constant and drops out of the equation. The resulting difference in the electrochemical potentials ΔE_{II-I} as a consequence of gas composition (i.e., the theoretical Nernst shift) yields a value of 80 mV. From the experiment (Figure 3), the measured Nernst shift can be extracted as follows: the half-cell potential for Ni(0)/Ni(II) on the green trace (99:1) of ≈ 21 mV can be estimated on the basis of the intermediate potential value between the Ni oxidation peak of the anodic sweep and the Ni reduction peak of the cathodic branch. By applying the same approach to the CV in the 9:1 mixture, the gray trace yields a value of ≈ 111 mV. The obtained experimental shift of ≈ 90 mV is therefore in a good agreement with the thermodynamic calculation. The minor deviation of ≈ 10 mV can be most likely explained on the basis of superimposed kinetic hysteresis effects.

2.3. Reactivity Analysis of the Ni- Versus $Ni_{80}Cu_{20}$-Thin-Film Electrodes

To account for reactivity differences of the Ni/8-YSZ versus $Ni_{80}Cu_{20}$/8-YSZ electrodes, the measured current was normalized with respect to the TPB length of each electrode, which was determined by SEM image analysis (Figure S4 and S5,
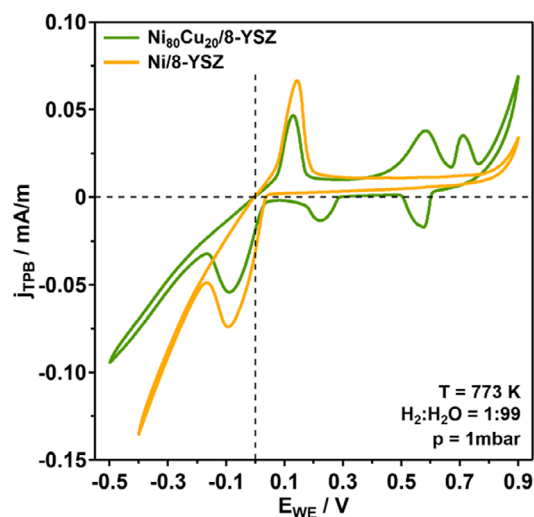
Figure 4. TPB-normalized current density j_{TPB} on the Ni/8-YSZ (orange trace) versus $Ni_{80}Cu_{20}$/8-YSZ electrode (green trace), measured as a function of potential (E_{WE}; scan speed $= 50$ mV s^{-1}) at 773 K in 1 mbar H_2:$H_2O = 1$:99 atmosphere.

Supporting Information). While masking individual YSZ areas in the SEM images, the circumference of these areas represents the interface of the (bi)metallic thin film and the YSZ substrate, being a measure for the TPB length (Table S1, Supporting Information). However, the purely geometric estimation of the TPB length neglects the effective width of the TBP, which acts as a interdiffusion zone of ionic transport within the YSZ/Ni(Cu) domains. Based on the structural and compositional similarities of both electrode systems, it can be nevertheless assumed that the TPB dimensions are at least similar.

Figure 4 presents a plot of the TPB-normalized current density (j_{TPB}) as a function of the potential (E_{WE}) and compares the activity differences of the electrode materials Ni/8-YSZ (orange trace) and $Ni_{80}Cu_{20}$/8-YSZ (green trace) at 773 K in 1 mbar H_2:$H_2O = 1$:99 atmosphere. In the cathodic branch approaching the hydrogen evolution reaction (HER), the pure Ni electrode shows higher current densities compared to the NiCu system. The higher activity of the Ni/8-YSZ electrode is most likely associated with the superior H_2 adsorption kinetics of metallic Ni, which become rather suppressed by the addition of Cu.[26] However, in the anodic branch, the NiCu alloy outperforms pure Ni and results in a higher electrocatalytic activity ($Ni_{80}Cu_{20} > Ni$) upon approaching the oxygen evolution reaction (OER). In this perspective, the beneficial role of Cu is not fully understood so far. However, the active phase in the onset region of the OER was identified to be a mixture of Ni(0), Ni oxides, and CuO (cf. Figure 3).

In essence, the data show how NAP–XPS functions as a fundamental spectroscopic tool to gain insights into electrochemically active surface states of high temperature solid oxide model cells under close-to-real operation conditions.

2.4. Product Tracking During HER

To deliver even further experimental proof of the versatility of our thin-film model cells, a kinetic operando measurement
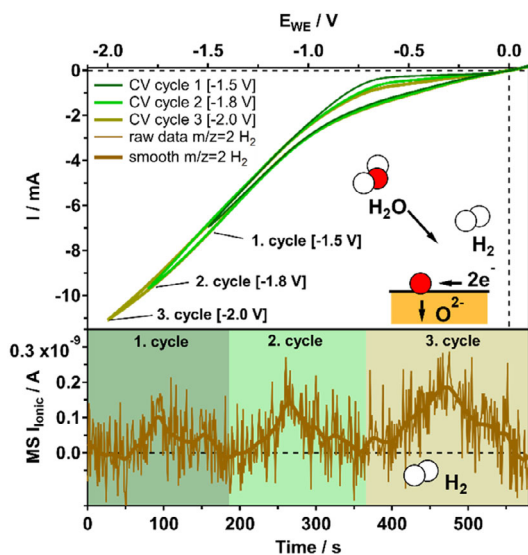
Figure 5. Top panel: cyclic voltammograms (20 mV s^{-1}, three cycles with decreasing vertex potentials as indicated in the legend) on the Ni$_{80}$Cu$_{20}$/8-YSZ electrode at 723 K in 1 mbar H$_2$:H$_2$O = 1:99 atmosphere. The lower panel depicts the correlation of hydrogen evolution ($m/z = 2$) with time during periodic CV cycling (brownish traces for raw and smoothed experimental quadrupole mass spectrometer [QMS] data).

complemented by online MS in the CV region of the HER was conducted (cf. Figure 4). The potential of the Ni$_{80}$Cu$_{20}$/8-YSZ electrode was swept cathodically with 20 mV s^{-1} at a temperature of 723 K in 1 mbar H$_2$O:H$_2$ = 99:1 atmosphere to trigger the electroreduction of water vapor according to Equation (4) at the WE:

$$H_2O + 2e^- \rightleftharpoons O^{2-} + H_2 \quad (4)$$

At the same time, the H$_2^+$ signal ($m/z = 2$) was recorded with the QMS located in the first pumping stage of the NAP–XPS apparatus, which directly senses the gases formed at the WE. The limit of the cathodic vertex potential was decreased in each subsequent CV cycle: i.e., cycle 1, dark green trace: −1.5 V; cycle 2, light green trace: −1.8 V; cycle 3, ochre-colored trace: −2.0 V. The obtained CV cycle data are plotted as E_{WE} versus I curves in **Figure 5** (top panel). The same color code is used to qualitatively relate the H$_2$ formation based on Equation (4), as detected by online QMS, to each corresponding CV cycle. The recorded H$_2$ intensity response ($m/z = 2$ signal as function of time) is represented in the bottom panel of Figure 5 as raw and smoothed experimental traces (brown). Clearly, this operando QMS measurement allows to correlate the decrease of the cathodic vertex potential and the associated increase of the cathodic current density with the growing amount of H$_2$ recorded in each CV cycle without any delay. Eventually, we suggest that even quantitative activity data are attainable on this basis, provided that the electrode activity is high enough to allow for an acceptable signal-to-noise ratio of the QMS signal.

3. Conclusions

Porous quasi-2D Ni and NiCu thin-film electrodes on polished YSZ substrates were prepared by metal (co-)evaporation to obtain homogeneous and flat (bi)metallic films, which can be transformed to more open holey or network-like (bi)metallic layers via controlled thermal annealing. These transformed layers offer a remarkable combination of high electronic conductivity and an abundance of spectroscopically accessible interface sites between the (bi)metallic layers and YSZ phases. They function as a spectroscopic window into the intricate world of local electrochemical phenomena, allowing us to study redox reactions and adsorbate chemistry close to the electrocatalytically relevant TPB by means of electron spectroscopic in situ and operando techniques (NAP–XPS). The insights gained from these quasi-2D porous systems are set to revolutionize our fundamental understanding of the TPB, where critical exchange processes occur in technologically relevant cermet electrode materials. Even subtle variations in gas composition and polarization result in spectroscopically sensitively measurable and well-reproducible electrochemical surface state responses and segregation trends, as demonstrated by the cyclic voltammetry (CV) patterns and the associated NAP–XPS data of this study. The microscopic determination of the TPB length (Table S1, Supporting Information) allows for a comparison of TPB-normalized electrocatalytic properties, and therefore, to rank the catalysts based on their activity, while at the same time tracking the electrocatalytically active surface states and compositions. With respect to electrochemical activity, the 2D-network thin-film cells exhibit an impressive level of exchange current density, especially for the HER from gaseous water. Together with the feasible quantification of electrochemical hydrogen formation via online QMS, while simultaneously recording XP or Auger spectra, true operando spectroscopic electrochemical studies are accessible.

Beyond the technologically most relevant Ni–YSZ system, we emphasize the versatility of the chosen thin-film approach toward more complex quasi-2D porous or network-like model electrodes, as a broad variety of mono- and bimetallic thin films on variable electrolyte substrates is accessible via the chosen preparation routine. The successful preparation and characterization of the bimetallic NiCu–YSZ model electrode represents a first showcase.

4. Experimental Section

Cell Preparation: The preparation of the button cells (Ø 5 mm) started with a commercial polycrystalline (ZrO$_2$)$_{0.92}$(Y$_2$O$_3$)$_{0.08}$ (8-YSZ) electrolyte substrate (Kerafol, Germany) with a thickness of 150 µm. The solid electrolyte was commercially coated on one side with a porous 10 mol% gadolinium-doped ceria Gd$_{0.1}$Ce$_{0.9}$O$_{1.95}$ (GDC-10) adhesion-promoting layer, on which the counter electrode (CE) was deposited. A Pt/GDC-10 cermet ink (volume ratio 52:48) was fabricated from Pt paste (Tanaka Kikinzoku Kogyo K.K., Tokyo, Japan), pre-sintered (12 h, 1123 K, 5% H$_2$ in He) GDC-10 nanopowder (Sigma Aldrich, 99.9 %), and 20 wt% terpineol as ink vehicle (Neyco, France). All reagents were mixed together and ball milled (ZrO$_2$ spheres) under 600 rpm for 15 min. The ink was then spin-coated (3000 rpm, 20 s) onto the GDC-10 adhesion-promoting layer and dried for 72 h at 393 K. Finally, the pure Pt paste diluted with a terpineol-based thinner (Tanaka, Japan) was paint brushed onto the dried Pt/GDC-10 cermet layer. After a second drying step (24 h, 393 K), the CE was sintered at

**ADVANCED
SCIENCE NEWS**

www.advancedsciencenews.com

**small
structures**

www.small-structures.com

1423 K in air for 3 h. The so-prepared CE exhibited particularly high electro-catalytic activity by combining high surface area with an optimized number of TPB sites. This well-established strategy for CE preparation reduced overpotentials relative to a thin-film-based WE to negligible values.[14] For the preparation of the WE, the uncoated side of the electrolyte substrate was gently grinded (SiC paper P4000) under ethanol and polished by means of an aqueous diamond suspension (grain diameters 3, 1, and 0.25 µm, Struers GmbH). After ultrasonic cleaning in 2-propanol and annealing at 873 K in air for 5 h, the cell was transferred for further coating into a vacuum chamber equipped with a dual evaporator unit for physical vapor co-deposition[28] (background pressure $\approx 1 \times 10^{-7}$ mbar) and fixed on a substrate heater. Nickel and copper (wires with Ø 1 mm, 99.9 % purity) were thermally evaporated from two alumina-coated Mo boats and deposited on the bare WE side of the heated 8-YSZ substrate ($T_{substrate} = 603$ K). A microbalance was used to monitor the deposited film thickness (100 nm) and deposition rate (2 nm min^{-1}). During sequential Ni/Cu co-evaporation, an alternating shutter shielded the respective boat. To fabricate a nominal composition of Ni$_{80}$Cu$_{20}$, 10 full growth cycles with 8 nm of Ni and 2 nm of Cu in each cycle were performed. The resulting layered, fully surface-covering (bi)metal film was then annealed under 50 mbar H$_2$ and 950 mbar He atmosphere in a quartz reactor at sufficiently high temperatures to obtain both complete NiCu intermixing and local de-wetting of the YSZ electrolyte substrate, leading to the formation of the desired nanoscaled, electronic conducting, cermet-like (bi)metallic network. A study from Gauckler et al.[19] allowed to roughly estimate the annealing temperature based on the melting point of the bi(metal) phase and the layer thickness. The refined annealing temperature was approached empirically by increasing the applied temperature stepwise (1073 K for the Ni electrode and 1043 K for the Ni$_{80}$Cu$_{20}$ electrode) and was chosen just high enough to crack the metal thin-film layer by means of beginning Ostwald ripening. By further increasing the annealing temperature (1123 and 1073 K, respectively), the network-like structure broke down, island-like features were formed and electronic conductivity was eventually lost. At the mentioned annealing temperatures (Ni: 1073 K and 1123 K; Ni$_{80}$Cu$_{20}$: 1043 K and 1073 K), a detailed structural, spectroscopic, and electrochemical characterization of the respective intact or broken thin-film electrode was conducted, as described later.

Characterization Methods: Hydrogen Annealing Treatment: The employed ultra-high vacuum setup[29] allowed for ex situ XPS characterization before and after sample treatment in an attached all-quartz recirculating batch reactor. Originally, it was designed for quantitative catalytic/kinetic reaction studies up to 1 bar total pressure, thereby detecting the reaction products by online MS analysis (Hewlett Packard gas chromatography–MS system G1800A) via a capillary leak. In the present study, the reaction cell was only used for thermal sample annealing under ultraclean conditions. For this, the samples were transferred to the reactor and an annealing procedure in 50 mbar H$_2$ and 950 mbar He was performed at the temperatures described in Section 1.2.1 before. For the annealing treatments, the reactor was heated with a constant linear rate of 10 K min^{-1} to the respective final temperatures and then kept isothermally at the respective temperature for 90 min.

Scanning Electron Microscopy and Energy-Dispersive X-Ray Spectroscopy: Scanning electron microscopy (SEM) and energy-dispersive X-ray spectroscopy (EDXS) analysis were carried out on an FEI Quanta 650 FEG, which was a field-emission SEM. The nonconductive samples were sputter-coated with Au to prevent charging. The microscope was operated with an electron acceleration voltage of 15 kV, while recording images under high vacuum (6×10^{-6} mbar). Elemental information was determined by EDXS measurements using an Oxford XMAX50 detector.

Atomic Force Microscopy: Atomic force microscopy (AFM) images were recorded in tapping mode with an amplitude of 1.2 V on a Dimension 3100 microscope (Veeco) using n-doped silicon probes (force constant: 20–80 N m^{-1}; resonance frequency: 256–317 kHz, RTESPW, Veeco). For all images, 1024 × 512 data points were recorded with a scan rate of 0.15 Hz. For data processing of AFM and SEM images, the software package Gwyddion was used.[30]

Operando NAP–XPS Combined with Online MS and Electrochemical Characterization: For electron-spectroscopic in situ/operando investigations under electrochemical reaction conditions, experiments in a custom-designed laboratory-based Specs NAP–XPS system were performed. The entire system is described in detail in ref. [31]. In brief, the central XPS setup comprised a µFOCUS 600 NAP monochromatic small spot (300 µm) Al–K$_{\alpha}$ X-ray source and a hemispherical energy analyzer (Specs Phoibos 150 NAP equipped with a 1D delay line detector) in vertical configuration within a µ-metal analysis chamber shielding the system from external electric and magnetic fields. The differentially pumped electrostatic lens system separates gas molecules from the photoelectrons focused toward the analyzer, which enabled XPS experiments during back-filling of the analysis chamber up to a pressure of 25 mbar with variable gases and gas mixtures supplied via mass flow controllers (Bronkhorst). To measure the gas phase composition and the products formed on the surface area being observed by in situ XPS, two quadrupole mass spectrometers (QMSs, Hiden HPR-40 and MKS Instruments e-vision2) were installed in the first and second differential pumping stage past the analyzer nozzle, respectively, and operated depending on the specific sensitivity requirements. Gases formed at the sample surface inside the recipient were pumped through the nozzle and could be detected online without delay, giving live information on product formation at the sample surface. An infra-red laser (max. 120 W) was attached to the bottom side of the analyzing chamber and allowed to precisely heat the samples from the backside via an 8 mm hole in the sample holder. The temperature was measured by a K-type Ni/NiCr thermocouple placed in vicinity of the surface region observed by XPS. To ensure uniform heat transfer across the WE, and thus WE surface temperature, the thermocouple was connected to an uncoated area of the pristine YSZ disc by H$_2$ sintering the wires onto the YSZ surface by means of a Ni-paste droplet. A schematic cross-section drawing of the cell mounted on the sample holder can be found in Figure S1, Supporting Information. For a detailed description of the custom-made sample holder designed specifically for solid-state electrochemical studies, we refer again to ref. [31].

For XPS analysis, the X-ray source was operated at 70 W and 13 kV, while the analyzer was set to a constant pass energy of 50 eV for all recorded spectra. All XPS data were analyzed using the CasaXPS software program, version 2.3.24 PR1.0 (Casa Software Ltd.).[32] For background correction, a Shirley background was applied to the Ni 2p spectra. The main Ni 2$p_{3/2}$ peak was assigned to a BE of 852.8 eV for the metallic component[33] and to 852.7 eV for the alloyed component (Ni$_{80}$Cu$_{20}$).[20] The kinetic energy (KE) of the Cu LMM Auger peaks as well as the BEs of the Cu 2$p_{3/2}$ components for Cu(I) and Cu(II) were derived from the respective Cu reference samples measured on the same instrument under otherwise identical conditions (Cu(I): LMM KE = 916.6 eV, 2$p_{3/2}$ BE = 932.9 eV; Cu(II): LMM KE = 917.7 eV, 2$p_{3/2}$ BE = 934.0 eV).[34,35] The Cu LMM Auger peak characteristics and the BE of the alloyed Cu(0) species were taken from an XPS study on Cu–Ni alloys by Kleiman et al. (Cu(0): LMM KE = 918.9 eV, 2$p_{3/2}$ BE = 932.6 eV).[20]

Supporting Information

Supporting Information is available from the Wiley Online Library or from the author.

Acknowledgements

the frame of project P36926-N "Optimization of carbon reactivity in methane dry reforming".

Conflict of Interest

The authors declare no conflict of interest.

Data Availability Statement

The data that support the findings of this study are available from the corresponding author upon reasonable request.

Keywords

model electrodes, near-ambient pressure X-ray photoelectron spectroscopy (NAP–XPS), NiCu, solid oxide cells, thin-films

[1] A. Hauch, R. Küngas, P. Blennow, A. B. Hansen, J. B. Hansen, B. V. Mathiesen, M. B. Mogensen, *Science* **2020**, *370*, 6118.

[2] F. Ramadhani, M. A. Hussain, H. Mokhlis, S. Hajimolana, *Renewable Sustainable Energy Rev.* **2017**, *76*, 460.

[3] V. Kyriakou, D. Neagu, E. I. Papaioannou, I. S. Metcalfe, M. C. M. van de Sanden, M. N. Tsampas, *Appl. Catal., B* **2019**, *258*, 117950.

[4] E. J. Crumlin, H. Bluhm, Z. Liu, *J. Electron. Spectrosc. Relat. Phenom.* **2013**, *190*, 84.

[5] A. Knop-Gericke, E. Kleimenov, M. Hävecker, R. Blume, D. Teschner, S. Zafeiratos, R. Schlögl, V. I. Bukhtiyarov, V. V. Kaichev, I. P. Prosvirin, A. I. Nizovskii, H. Bluhm, A. Barinov, P. Dudin, M. Kiskinova, in *Advances in Catalysis*, Vol. *52*, Academic Press, Cambridge, US **2009**, pp. 213–272.

[6] D. E. Starr, Z. Liu, M. Hävecker, A. Knop-Gericke, H. Bluhm, *Chem. Soc. Rev.* **2013**, *42*, 5833.

[7] Z. Cheng, M. Liu, *Solid State Ionics* **2007**, *178*, 925.

[8] Z. Cheng, J.-H. Wang, Y. Choi, L. Yang, M. C. Lin, M. Liu, *Energy Environ. Sci.* **2011**, *4*, 4380.

[9] J. Kirtley, A. Singh, D. Halat, T. Oswell, J. M. Hill, R. A. Walker, *J. Phys. Chem. C* **2013**, *117*, 25908.

[10] A. Nenning, A. K. Opitz, C. Rameshan, R. Rameshan, R. Blume, M. Hävecker, A. Knop-Gericke, G. Rupprechter, B. Klötzer, J. Fleig, *J. Phys. Chem. C* **2016**, *120*, 1461.

[11] A. K. Opitz, A. Nenning, C. Rameshan, R. Rameshan, R. Blume, M. Hävecker, A. Knop-Gericke, G. Rupprechter, J. Fleig, B. Klötzer, *Angew. Chem., Int. Ed.* **2015**, *54*, 2628.

[12] S. B. Adler, *Solid State Ionics* **2000**, *135*, 603.

[13] S. Dierickx, T. Mundloch, A. Weber, E. Ivers-Tiffée, *J. Power Sources* **2019**, *415*, 69.

[14] J. Fleig, F. S. Baumann, V. Brichzin, H. R. Kim, J. Jamnik, G. Cristiani, H. U. Habermeier, J. Maier, *Fuel Cells* **2006**, *6*, 284.

[15] A. K. Opitz, J. Fleig, *Solid State Ionics* **2010**, *181*, 684.

[16] A. K. Opitz, A. Lutz, M. Kubicek, F. Kubel, H. Hutter, J. Fleig, *Electrochim. Acta* **2011**, *56*, 9727.

[17] F. El Gabaly, K. F. McCarty, H. Bluhm, A. H. McDaniel, *Phys. Chem. Chem. Phys.* **2013**, *15*, 8334.

[18] S. Vafaeenezhad, A. R. Hanifi, M. A. Laguna-Bercero, T. H. Etsell, P. Sarkar, *Futures* **2022**, *1*, 042101.

[19] T. Ryll, H. Galinski, L. Schlagenhauf, P. Elser, J. L. M. Rupp, A. Bieberle-Hutter, L. J. Gauckler, *Adv. Funct. Mater.* **2011**, *21*, 565.

[20] P. F. Barbieri, A. de Siervo, M. F. Carazzolle, R. Landers, G. G. Kleiman, *J. Electron. Spectrosc. Relat. Phenom.* **2004**, *135*, 113.

[21] A. Jablonski, C. Powell, *NIST Electron Inelastic-Mean-Free-Path Database, SRD 71*, Vol. *1.2*, National Institute of Standards and Technology, Gaithersburg, MD **2010**.

[22] M. C. Biesinger, L. W. M. Lau, A. R. Gerson, R. S. C. Smart, *Appl. Surf. Sci.* **2010**, *257*, 887.

[23] J. Kunze, V. Maurice, L. H. Klein, H.-H. Strehblow, P. Marcus, *Corros. Sci.* **2004**, *46*, 245.

[24] M. C. Biesinger, B. P. Payne, L. W. M. Lau, A. Gerson, R. S. C. Smart, *Surf. Interface Anal.* **2009**, *41*, 324.

[25] A. P. Grosvenor, M. C. Biesinger, R. S. C. Smart, N. S. McIntyre, *Surf. Sci.* **2006**, *600*, 1771.

[26] Y. Yao, D. W. Goodman, *J. Mol. Catal. A: Chem.* **2014**, *383–384*, 239.

[27] I. Zegkinoglou, L. Pielsticker, Z.-K. Han, N. J. Divins, D. Kordus, Y.-T. Chen, C. Escudero, V. Pérez-Dieste, B. Zhu, Y. Gao, B. R. Cuenya, *J. Phys. Chem. C* **2019**, *123*, 8421.

[28] T. Götsch, E.-M. Wernig, B. Klötzer, T. Schachinger, J. Kunze-Liebhäuser, S. Penner, *Rev. Sci. Instrum.* **2019**, *90*, 023902.

[29] L. Mayr, R. Rameshan, B. Klötzer, S. Penner, C. Rameshan, *Rev. Sci. Instrum.* **2014**, *85*, 055104.

[30] D. Nečas, P. Klapetek, *Open Phys.* **2012**, *10*, 181.

[31] L. Haug, C. Griesser, C. W. Thurner, D. Winkler, T. Moser, M. Thaler, P. Bartl, M. Rainer, E. Portenkirchner, D. Schumacher, *Rev. Sci. Instrum.* **2023**, *94*, 065104.

[32] J. Walton, P. Wincott, N. Fairley, A. Carrick, in *Peak Fitting With CasaXPS*, Accolyte Science, Knutsford, UK **2010**.

[33] M. Romand, M. Roubin, J. P. Deloume, *J. Electron. Spectrosc. Relat. Phenom.* **1978**, *13*, 229.

[34] C. W. Thurner, N. Bonmassar, D. Winkler, L. Haug, K. Ploner, P. Delir Kheyrollahi Nezhad, X. Drexler, A. Mohammadi, P. A. van Aken, J. Kunze-Liebhäuser, A. Niaei, J. Bernardi, B. Klötzer, S. Penner, *ACS Catal.* **2022**, *12*, 7696.

[35] C. W. Thurner, X. Drexler, L. Haug, D. Winkler, J. Kunze-Liebhäuser, J. Bernardi, B. Klötzer, S. Penner, *Appl. Catal., B* **2023**, *331*, 122693.